nanomaterials

MDPI

Article

WSe_2/g-C_3N_4 for an In Situ Photocatalytic Fenton-like System in Phenol Degradation

Li Tan [1,2], Yiming Chen [1,2], Didi Li [1,2], Shaobin Wang [3,*] and Zhimin Ao [1,2,4,*]

1 Guangdong-Hong Kong-Macao Joint Laboratory for Contaminants Exposure and Health, Guangzhou Key Laboratory Environmental Catalysis and Pollution Control, Institute of Environmental Health and Pollution Control, Guangdong University of Technology, Guangzhou 510006, China
2 Guangdong Key Laboratory of Environmental Catalysis and Health Risk Control, Key Laboratory for City Cluster Environmental Safety and Green Development of the Ministry of Education, School of Environmental Science and Engineering, Guangdong University of Technology, Guangzhou 510006, China
3 School of Chemical Engineering and Advanced Materials, The University of Adelaide, Adelaide, SA 5005, Australia
4 Advanced Interdisciplinary Institute of Environment and Ecology, Beijing Normal University, Zhuhai 519087, China
* Correspondence: shaobin.wang@adelaide.edu.au (S.W.); zhimin.ao@bnu.edu.cn (Z.A.)

Abstract: An in situ photo-Fenton system can continuously generate H_2O_2 by photocatalysis, activating H_2O_2 in situ to form strong oxidizing ·OH radicals and degrading organic pollutants. A WSe_2/g-C_3N_4 composite catalyst with WSe_2 as a co-catalyst was successfully synthesized in this work and used for in situ photo-Fenton oxidation. The WSe_2/g-C_3N_4 composite with 7% loading of WSe_2 (CNW2) has H_2O_2 production of 35.04 μmol/L, which is fourteen times higher than pure g-C_3N_4. The degradation efficiency of CNW2 for phenol reached 67%. By constructing an in situ Fenton-system, the phenol degradation rate could be further enhanced to 90%. WSe_2 can enhance the catalytic activity of CNW2 by increasing electron mobility and inhibiting the recombination of photogenerated electron–hole pairs. Moreover, the addition of Fe^{2+} activates the generated H_2O_2, thus increasing the amount of strong oxidative ·OH radicals for the degradation of phenol. Overall, CNW2 is a promising novel material with a high H_2O_2 yield and can directly degrade organic pollutants using an in situ photo-Fenton reaction.

Keywords: WSe_2/g-C_3N_4; visible light; in situ photo-Fenton; phenol degradation

Citation: Tan, L.; Chen, Y.; Li, D.; Wang, S.; Ao, Z. WSe_2/g-C_3N_4 for an In Situ Photocatalytic Fenton-like System in Phenol Degradation. *Nanomaterials* **2022**, *12*, 3089. https://doi.org/10.3390/nano12183089

Academic Editors: Detlef W. Bahnemann and Giuseppe Cappelletti

Received: 8 August 2022
Accepted: 2 September 2022
Published: 6 September 2022

1. Introduction

Phenol is a major pollutant in industrial wastewater such as oil refineries, petrochemical plants, coking plants, and phenolic resin plants [1]. Phenol may be produced in certain agricultural products and animal manure as well [2]. Phenol is a highly toxic organic pollutant that poses a health threat to humans and biota [3]. In recent decades, advanced oxidation processes (AOPs) have proven attractive for wastewater treatment [4]. Thus far, AOPs have been successfully applied to the degradation of persistent organic pollutants, and can convert toxic organic pollutants into easily degradable low molecular weight metabolites [5]. As a typical kind of AOP, Fenton reaction can take advantage of Fe^{2+} to activate hydrogen peroxide (H_2O_2) in order to form ·OH radicals, as shown in Equation (1).

$$Fe^{2+} + H_2O_2 \rightarrow Fe^{3+} + \cdot OH + OH^- \quad (1)$$

·OH can be used as an unselective reactive oxygen species (ROS) to degrade most organic pollutants in aqueous solutions [6]. Early in 1992, Zepp et al. [7] studied the kinetic mechanism of organic pollutants removal, including oxalate, citrate, and phosphate complexes through a photo-Fenton system constructed by Fe^{2+}. This has been the foundation for subsequent research on the photo-Fenton reaction in pollutant removal. The traditional

photo-Fenton reaction requires the addition of H_2O_2, which increases costs and limits its practical application. In contrast to the conventional Fenton reaction, which requires the addition of H_2O_2, an in situ photo-Fenton system can continuously generate H_2O_2 by photocatalysis and activate H_2O_2 in situ to form strong oxidizing ·OH radicals, accelerating the degradation of various pollutants [8,9]. In the in situ photo-Fenton system, the role of the catalyst is very important, as it is related to the production of H_2O_2 and the degradation of pollutants. Therefore, developing a photocatalyst to construct an in situ photo-Fenton system with high reactivity to produce H_2O_2 is critical for the degradation of pollutants.

Among various visible light-responsive materials, graphitized carbon nitride (g-C_3N_4) has attracted much attention because of its effective visible light absorption, suitable conduction band edge, high stability, and excellent environmental friendliness [10–13]. In 2014, Shiraishi et al. [14] discovered that g-C_3N_4 can be used as a photocatalyst for H_2O_2 production thanks to its high selectivity in ethanol/water mixed solutions when exposed to visible light ($\lambda > 420$ nm). Many subsequent studies have confirmed these findings [15–17]. However, bulk g-C_3N_4 usually exhibits poor photocatalytic activity owing to the low separation and transfer efficiency of photo-generated carriers [18]. Therefore, a series of modifications have been made to g-C_3N_4 to improve its photocatalytic activity.

Developing a precious metal-free co-catalyst with g-C_3N_4 as a composite material is a potential modification approach [19,20]. In recent years, transition metal dichalcogenides (TMDs) have attracted wide attention due to their unique layered structure, high stability, and excellent electronic and electro-optical properties [21,22]. Tungsten selenite (WSe_2) is a type of TMD that is widely used in energy and environmental areas, including in photodetectors [23], field-effect transistors [24,25], photocatalytic CO_2 reduction reactions (CO_2RR) [26], and water splitting [27]. Guo et al. [28] found that using WSe_2 nanosheets as a co-catalyst significantly increased the rate of photocatalytic H_2 production by $Zn_{0.1}Cd_{0.9}S$ nanorods. With visible light as a driver, the generation rate of H_2 was 147.32 mmol h^{-1} $g_{cat}{}^{-1}$, which is eleven times the initial ate of $Zn_{0.1}Cd_{0.9}S$. Similarly, Lin et al. [29] reported a floating plate photocatalytic system with WSe_2 as the co-catalyst which had an H_2 evolution rate of 64.85 mmol h^{-1} g^{-1}. These results suggest that WSe_2 is an effective co-catalyst that can act as an electron absorber to accelerate the separation of space carriers, thereby enhancing the performance of the photocatalytic reaction [30]. Wang et al. [30] synthesized a WSe_2/g-C_3N_4 photocatalyst which showed high H_2O_2 production and high bacterial inactivation efficiency. However, research on WSe_2 nanosheets as co-catalysts for photocatalytic organic pollutant removal is rarely reported.

In this work, WSe_2/g-C_3N_4 composite catalysts with WSe_2 as a co-catalyst were successfully synthesized by a hydrothermal method combined with a calcination method. The photocatalytic H_2O_2 production and the degradation of phenol with pure g-C_3N_4 and the WSe_2/g-C_3N_4 composite catalysts were tested in pure water under visible light. At the same time, Fe^{2+} was added to create an in situ optical Fenton system for phenol degradation. Coumarin was used as a trap to detect the ·OH produced by the photocatalytic reaction. This work shows that the WSe_2/g-C_3N_4 composite is a potential photocatalyst that can produce H_2O_2 in pure water and be directly used in an in situ photo-Fenton reaction to degrade organic pollutants.

2. Materials and Methods

2.1. Chemicals and Materials

Melamine ($C_3H_6N_6$ 99%, analytically pure) was obtained from Shanghai Macklin Biochemical Technology Co., Ltd., Shanghai, China. Selenium powder, sodium tungstate dihydrate ($Na_2WO_6{\cdot}2H_2O$ 99.5%, analytically pure), sodium borohydride ($NaBH_4$, analytically pure), tungsten selenide (WSe_2 99%, analytically pure), ferrous sulfate heptahydrate ($FeSO_4{\cdot}7H_2O$ > 99%, analytically pure), phenol (C_6H_6O, analytically pure), horseradish peroxidase (POD, RZ > 3.0), N,N-diethyl-p-phenylenediamine sulfate salt (DPD), and coumarin ($C_9H_6O_2$ 99%, analytically pure) were all provided by Shanghai Aladdin Biochemical Technology Co., Ltd., Shanghai, China. N,N-dimethylformamide

(C_3H_7NO, analytically pure) was purchased from Guangzhou Chemical Reagent Factory, Guangzhou, China. Ultra-pure water was used in all experiments.

2.2. Synthesis

Preparation of g-C_3N_4: The original g-C_3N_4 (labeled as PCN) was prepared by thermally polymerizing melamine [31]. The specific experimental operation is as follows: 10 g of $C_3H_6N_6$ powder was placed into a crucible, then the crucible was heated under 520 °C for 2 h in a box furnace. After the sample was naturally cooled, a yellow solid was obtained and was collected after grinding.

Preparation of WSe_2/g-C_3N_4: According to the previous method [30], several WSe_2/g-C_3N_4 composite materials with different ratios were synthesized by the combination of a hydrothermal and calcination method. The specific experimental operation was as follows: a mixture of selenium powder (Se, 57.7 mg, 0.731 mmol) and sodium tungstate dihydrate ($Na_2WO_6 \cdot 2H_2O$, 120.75 mg, 0.366 mmol) was added to a beaker containing N, N-dimethylformamide (DMF, 60 mL). Then, 100 mg of sodium borohydride ($NaBH_4$) was slowly added under constant stirring, and the mixture solution was continuously stirred for 2 h. After that, 2.5 g of PCN was added to the above mixed solution and stirred for 1 h. After the stirring, the solution was transferred into a closed autoclave with a volume of 100 mL and went subjected to heat treatment at 240 °C for 24 h. The solution was cooled to room temperature and washed with ultrapure water and absolute ethanol several times, then dried under vacuum at 60 °C for 24 h. Finally, the obtained solid was ground into powder, which was calcined and annealed in a tube furnace at 300 °C for 5 h under an argon atmosphere. The WSe_2/g-C_3N_4 material with a WSe_2 loading of 5% was named as CNW1. To determine the WSe_2/g-C_3N_4 material with the best photocatalytic performance, other samples with 7%, 10%, and 14% loadings of WSe_2 were prepared. These materials were marked as CNW2, CNW3, and CNW4, respectively.

Preparation of WSe_2: A mixture of Se powder (315.6 mg, 4 mmol) and $Na_2WO_6 \cdot 2H_2O$ (659.6 mg, 2 mmol) was added to a beaker containing 60 mL DMF while stirring. Then, 100 mg $NaBH_4$ was slowly added into the mixed solution and stirred continuously for 3 h. The rest of the operation was the same as the preparation method used for WSe_2/g-C_3N_4.

2.3. Characterizations

X-ray diffraction (XRD) patterns of the synthesized materials were obtained from an X-ray diffractometer with a Cu-Kα radiation source (λ = 1.5218 Å) (D8 ADVANCE, Bruker Inc., Saarbrucken, Germany). Transmission electron microscopy (TEM) images were examined on a Talos F200S (FEI, Thermo, Inc., Czech Republic) field-emission transmission electron microscope operated at 200 kV. Field emission scanning electron microscopy (FESEM) with energy dispersive X-ray spectroscopy (EDX) elemental mapping images were taken by a field-emission electron microscope (SU8220, Hitachi Ltd., Tokyo, Japan) with an acceleration voltage of 15 kV. X-ray photoelectron spectroscopy (XPS) spectra were obtained from a Escalab 250Xi (Thermo Fisher Scientific, Inc., Waltham, MA, USA) spectrometer with Al Kα radiation. Photoluminescence (PL) spectra were obtained using an FS5 (Edinburgh Inc., Edinburgh, UK) fluorescence spectrophotometer under 380 nm excitation. UV–vis diffuse reflectance spectra (UV–vis DRS) were acquired on a Cary 300 spectrophotometer (Agilent Technologies Inc., Palo Alto, CA, USA).

2.4. Photocatalytic Performance

Photocatalytic production of H_2O_2: This experiment was carried out in a PCX50B Discover multi-channel photocatalytic system (5 W, λ > 420 nm, Perfectlight Technology Co., Ltd., Beijing, China). Typically, a catalyst sample (30 mg) was added to a reactor containing 30 mL of pure water. Before being exposed to light, a dark adsorption treatment was carried out for 30 min. Then, the light was turned on and the reaction proceeded for 2 h. During the photocatalytic reaction, 1 mL of the solution was collected every 20 min and filtered through a polytetrafluoroethylene (PES) millipore filter (0.22 μm) to remove

the photocatalyst powders. Finally, the amount of H_2O_2 produced by photocatalysis was determined by the DPD-POD method [32]. The specific method was as follows: 1 mL of sample aliquots were mixed with 1.12 mL water, 0.4 mL phosphate buffered solution, 0.05 mL POD (1 mg/mL^{-1}), and 0.05 mL DPD (10 mg/mL). Vigorous stirring was maintained for 1 min, then the absorbance of the mixed liquid was measured at 551 nm on a multifunctional microplate reader (Varioskan LUX, Thermo Fisher Scientific, Inc., Waltham, MA, USA). To ensure the accuracy of the experiment, the absorbance of H_2O_2 was measured three times.

Photocatalytic degradation of phenol: In this experiment, phenol with a concentration of 10 ppm (10 mg/L) was used as the target pollutant. The phenol degradation performance of the prepared photocatalysts was tested under the visible light irradiation of the PCX50B Discover multi-channel photocatalytic system. A catalyst sample (30 mg) was added to a reactor with 30 mL of phenol solution (10 ppm). Before exposure to light, a dark adsorption treatment was carried out for 30 min. Then, the light was turned on and the reaction proceeded for 6 h. During the photocatalytic reaction process, water samples were taken every 1 h. The solution was transferred into a high-performance liquid chromatography (HPLC, Eclassical 3100, Elite Analytical Instrument Co., Ltd., Dalian, China) vial, and the concentration of phenol was analyzed and determined by HPLC equipment with a UV detector. Methanol and ultra-pure water (40:60) were employed as the mobile phases at a flow rate of 0.8 mL min^{-1} and the wavelength of the detector was set at 270 nm. The degradation rate of phenol can be expressed by Equation (2)

$$D = 1 - \left(\frac{C}{C_0}\right) \times 100\% \quad (2)$$

where C and C_0 represent the concentrations of phenol at a specific interval and the initial time, respectively [33].

In situ photo-Fenton degradation of phenol: The H_2O_2 generated by photocatalysis was activated in situ by adding an external iron source to form an in situ photo-Fenton system. Generally, a catalyst sample (30 mg) was added to a reactor with 30 mL phenol solution (10 ppm). Before exposure to light, a certain amount of ferrous sulfate heptahydrate ($FeSO_4 \cdot 7H_2O$) solid was added into the reactor, then a dark adsorption experiment was carried out for 30 min. The operations of sampling and phenol concentration measurement were the same as described above.

Detection of hydroxyl radicals (·OH): Coumarin was used as a trap to detect the hydroxyl radicals produced in the photocatalytic reaction [34]. In detail, a catalyst sample (30 mg) was added into a reactor containing 30 mL coumarin (1 mM) solution. Before exposure to light, a dark adsorption treatment was carried out for 30 min. During the photocatalytic reaction, samples were taken every 20 min. Finally, the fluorescence spectrum of the solution was measured with a fluorescence spectrometer with a wavelength of 332 nm.

3. Results and Discussion

3.1. Characterizations of Materials

X-ray diffraction was used to investigate the crystal structure of diverse materials. The XRD spectra of pure WSe_2, PCN, CNW1, CNW2, CNW3, and CNW4 are shown in Figure 1a. The XRD spectrum of the pure WSe_2 is well matched with its standard card (JCPDS: 38-1388) [35], indicating that WSe_2 can be synthesized by this method with high purity. The XRD patterns of the CNW materials are nearly identical to PCN, demonstrating that the addition of WSe_2 does not affect the crystal structure of PCN. There are two characteristic peaks in the spectra of PCN and CNW materials. The peak at 13.1° corresponds to the (100) plane of PCN, representing the repetition of non-planar units. The other peak at 27.5° corresponds to the (002) plane of PCN, which is related to the superimposed reflection of the conjugate plane [36]. In addition, as WSe_2 loading in CNW composites increases, the intensity of the (100) and (002) peaks gradually weakens. The insignificant peak of WSe_2 in the CNW materials is due to the low content of WSe_2.

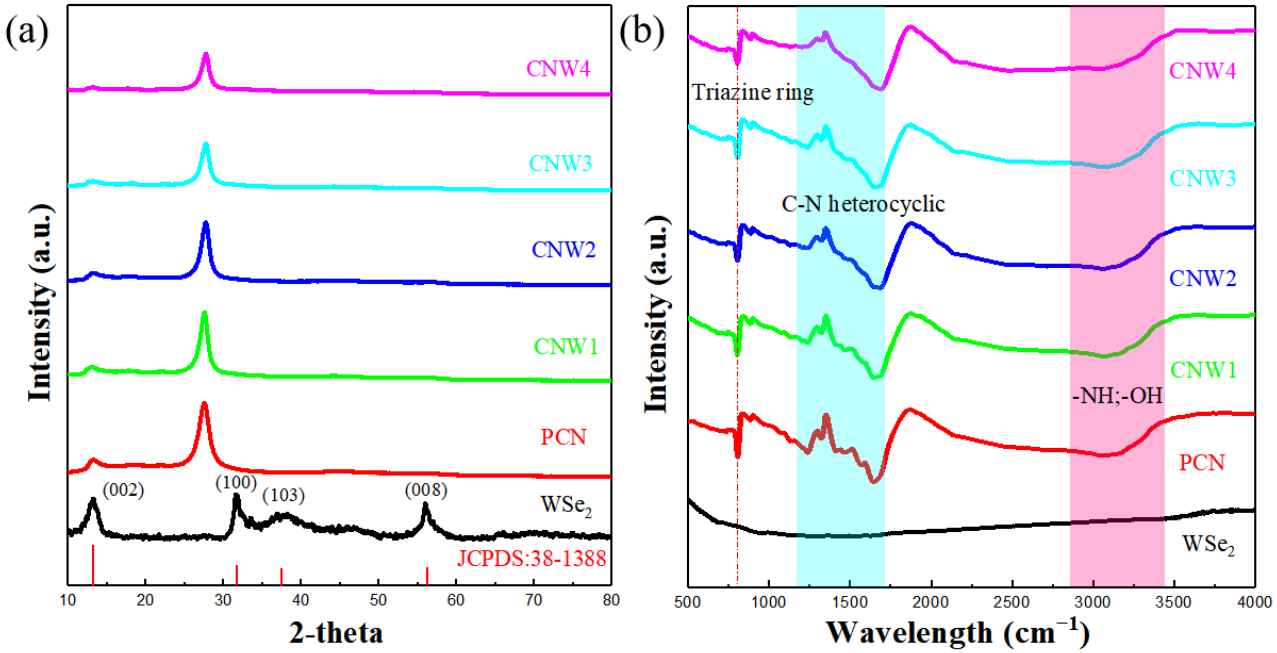

Figure 1. (**a**) XRD spectra and (**b**) FTIR spectra of pure WSe_2, PCN, CNW1, CNW2, CNW3, and CNW4.

The FTIR spectra of pure WSe_2, PCN, CNW1, CNW2, CNW3, and CNW4 are shown in Figure 1b. There is no clear sharp peak in the infrared spectrum of WSe_2 across the full wavenumber range (500–3500 cm^{-1}). The spectrum of CNW composite materials is similar to that of PCN, which indicates that PCN is the primary source of the infrared spectrum signals in CNWs. A tiny peak appearing at 810 cm^{-1} is attributed to the vibration of the triazine unit in PCN and CNW materials. The characteristic peak in the region of 1200–1700 cm^{-1} can be assigned to the C–N heterocyclic ring frame stretching vibration [37,38]. In addition, the characteristic peaks between 3000–3400 cm^{-1} can be assigned to the stretching vibrations of –OH and –NH groups caused by free amino groups in the PCN structure and hydroxyl groups adsorbed on the surface [39].

For the practical study of materials, thermal stability is essential. The TGA plots of the materials were tested in N_2 atmosphere. All of the produced materials exhibit excellent thermal stability in the 30~500 °C range, as shown in Figure S1. This demonstrates that it is feasible to use CNW materials to treat pollutants in water. The specific surface area of PCN and CNW2 are determined by the nitrogen adsorption–desorption isotherm. As shown in Figure S2, the specific surface area of PCN and CNW2 fitted with the Brunauer–Emmett–Teller (BET) method are 4.61 m^2/g and 11.83 m^2/g, respectively. The tiny BET surface area may have little influence on the catalytic activity for H_2O_2 evolution or phenol degradation, similar to the results in the literature [30].

The morphology of the synthesized samples was obtained by SEM. As shown in Figure 2a, PCN has a large irregular block structure and a relatively smooth surface. In Figure 2b, the synthesized WSe_2 exhibits a layered petal-like structure self-assembled from ultra-thin nanosheets, consistent with previous studies [40]. Figure 2c,d suggests a few ultra-thin WSe_2 nanosheets grown on the surface and edges of PCN, which indicates that the WSe_2 nanosheets were successfully loaded. The WSe_2 and PCN in the CNW2 are in close contact, which promotes the rapid transfer of photogenerated electrons from the surface of the PCN to the WSe_2. The distribution of various elements (C, N, W, Se) in CNW2 was studied by element mapping analysis. From the HAADF-SEM and the corresponding EDX elemental mapping images of CNW2 (Figure 2e,f), CNW2 contains four elements, i.e., C, N, W, and Se, and their uniform distribution indicates that CNW

nanocomposites were successfully prepared. The SEM image and the corresponding EDX elemental mapping images of PCN, CNW3, and CNW4 are shown in Figure S3.

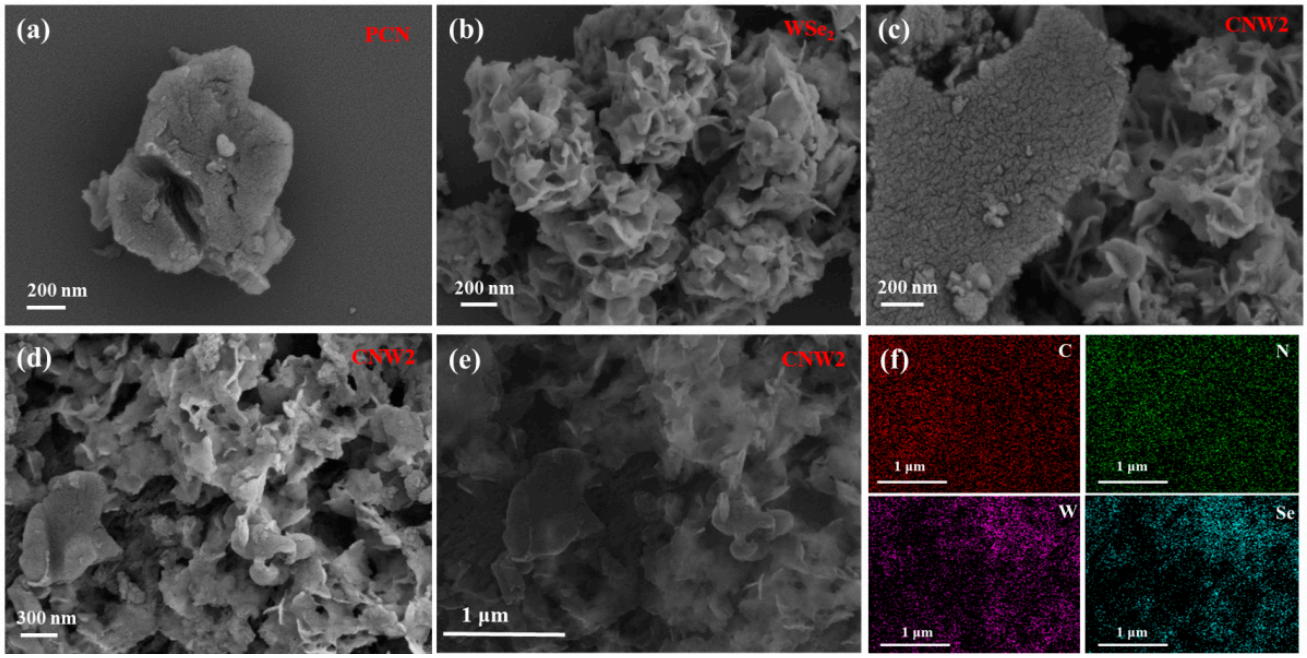

Figure 2. SEM images of (**a**) PCN, (**b**) WSe_2, and (**c**,**d**) CNW2; (**e**) HAADF-SEM image and (**f**) corresponding EDX elemental mapping images of CNW2.

The micromorphology of PCN and CNW composite materials were further analyzed by TEM and HRTEM (Figure 3 and Figure S4). As shown in Figure S4a,b, there are no lattice fringes locally due to the low crystallinity of PCN. As shown in Figure 3a, WSe_2 nanosheets are mainly loaded on the edge of g-C_3N_4. WSe_2 exhibits distinct lattice fringes with a fringe spacing of about 0.68 nm, corresponding to the (002) crystal plane of WSe_2 [40,41]. Moreover, the size of WSe_2 nanosheets is approximately 30 nm, much smaller than the size of PCN nanosheets. These results reveal that the WSe_2 nanosheets were successfully loaded onto the PCN, which is consistent with the SEM observations.

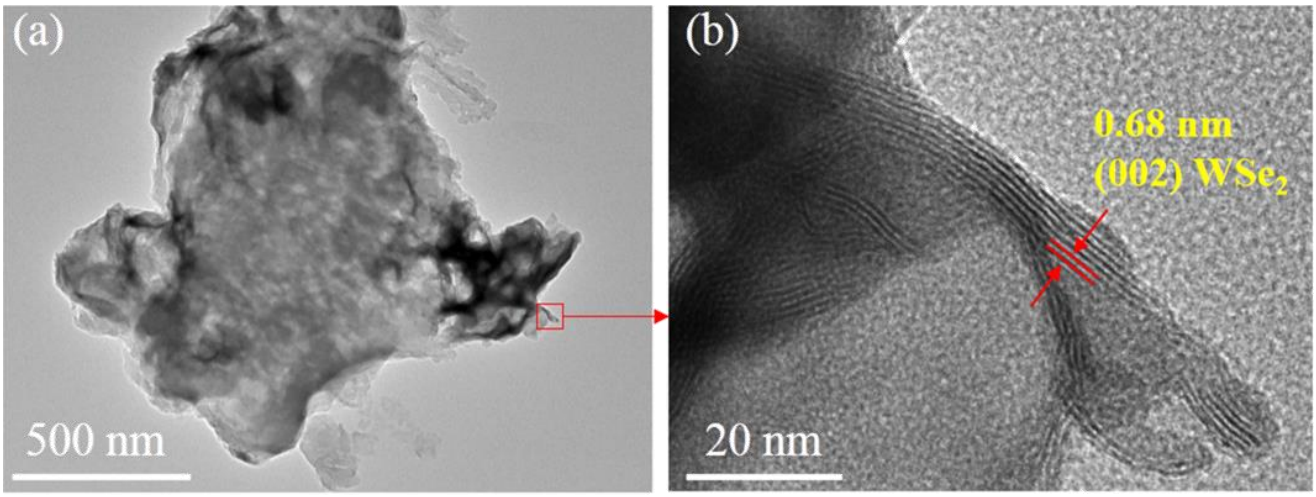

Figure 3. (**a**) TEM image of CNW2 and (**b**) HRTEM image of CNW2.

The XPS survey spectra of WSe_2, CNW2, and PCN are shown in Figure 4a. The characteristic peaks of the four elements, C, N, W, and Se, can be observed from the XPS

spectrum of the CNW2 composite material, which is consistent with the EDX element mapping. The XPS spectrum of CNW2 is similar to that of PCN, because PCN is the major component of CNW2. Because the relative content of WSe_2 in CNW2 composites is relatively small, the characteristic peaks of W and Se in the XPS spectra of the CNW2 composites are very weak.

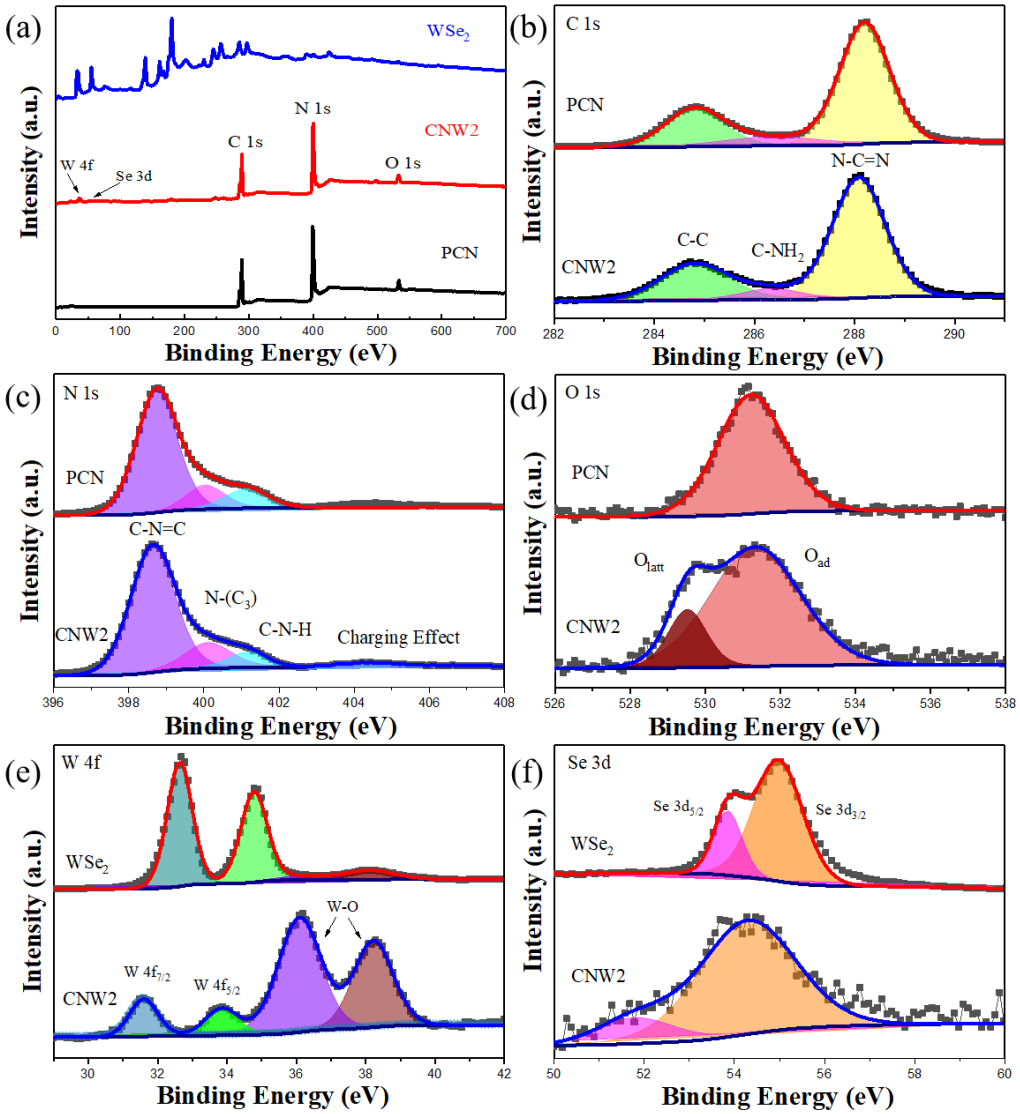

Figure 4. (**a**) XPS survey spectra of WSe_2, CNW2, and PCN, (**b**) High-resolution XPS C 1s spectra of CNW2 and PCN, (**c**) N 1s spectra of CNW2 and PCN, (**d**) O 1s spectra of CNW2 and PCN, (**e**) W 4f spectra of WSe_2 and CNW2, and (**f**) Se 3d spectra of WSe_2 and CNW2.

Figure 4b–f shows the high-resolution XPS spectra of C 1s, N 1s, O 1s, W 4f, and Se 3d from WSe_2, CNW2, and PCN. In the XPS spectra of C 1s, the characteristic peak at the binding energy of 284.8 eV corresponds to the extraneous carbon element (C–C bond). Normally, the two peaks at 286.4 and 288.2 eV in PCN are attributed to the C–NH_2 and N–C=N bonds, respectively [42,43], while in CNW2 composites these two peaks are negatively shifted by 0.1 eV compared to PCN, being located at 286.3 and 288.1 eV, respectively. In Figure 4c, the strongest characteristic peak of PCN located at the binding energy of 398.7 eV indicates the presence of sp^2 hybrid nitrogen on the aromatic ring of the N atom (C–N=C) [44]. The peak near the binding energy of 400.1 eV is attributed to the tertiary nitrogen N–$(C)_3$ group [45]. In addition, two weak peaks at the binding energy of 401.2 and 404.4 eV are attributed to the amino group (C–N–H) and the charging effect in the heterocyclic ring,

respectively [42,46]. Similarly, after WSe_2 loading, the four peaks are all transferred to the lower binding energy positions (398.6, 400.0, 401.1, and 404.3 eV). The XPS spectrum of O 1s is shown in Figure 4d. The peak of CNW2 and PCN at the binding energy of about 532.3 eV is considered to be the adsorbed oxygen species [47]. There is a new peak in the CNW2 composite material appearing at the binding energy of 529.4 eV which can be assigned to the lattice oxygen atom [48], which indicates that the surface of WSe_2 in the CNW2 composite is slightly oxidized.

As shown in Figure 4e, four typical peaks in WSe_2 nanosheets are located at the binding energy of 32.5, 34.6, 36.9, and 38.9 eV, respectively. The first two peaks can be attributed to W $4f_{7/2}$ and W $4f_{5/2}$ of W^{4+} in pure WSe_2, respectively. The other two small double peaks can be attributed to the W–O bond, which may be due to the oxidation state of W^{6+} formed by slight oxidation on the surface of the WSe_2 nanosheets during the synthesis process [49–51]. In CNW2 composites, these peaks are all shifted to the lower binding energy positions (31.7, 34.0, 36.2, and 38.4 eV). In addition, the proportion of the W–O peak area of WSe_2 in CNW2 composites increases due to the loading of WSe_2 nanosheets on the surface of PCN. Figure 4f shows that the Se 3d spectrum in WSe_2 can be divided into Se $3d_{5/2}$ (54.9 eV) and Se $3d_{3/2}$ (55.8 eV) of the divalent Se ion, which is consistent with previous studies [52,53]. In the CNW2 composite, Se $3d_{5/2}$ and Se $3d_{3/2}$ move to positions with binding energies of 51.9 and 54.8 eV, respectively. The changes in the binding energy of these chemical bonds indicate that electrons are transferred from PCN to WSe_2 nanosheets in the CNW2 samples. Due to the strong Mott–Schottky effect between PCN and WSe_2, the electron density of WSe_2 increases, affecting the electronic structure of the two materials.

As shown in Figure 5a, PCN exhibits an absorption band at around 450 nm while pure WSe_2 has a broad and strong absorption range across the full wavelength (300–800 nm). The visible light capturing ability of CNWs is significantly better than PCN due to the addition of WSe_2. These changes can be further verified by the changes in the physical appearance of the various samples. As shown in Figure 5b, the increasing content of WSe_2 in CNW samples causes their color to change from yellow to dark yellow and finally to black. The high light absorption capacity of the CNWs could promote the reaction of photocatalytic H_2O_2 production and pollutant degradation.

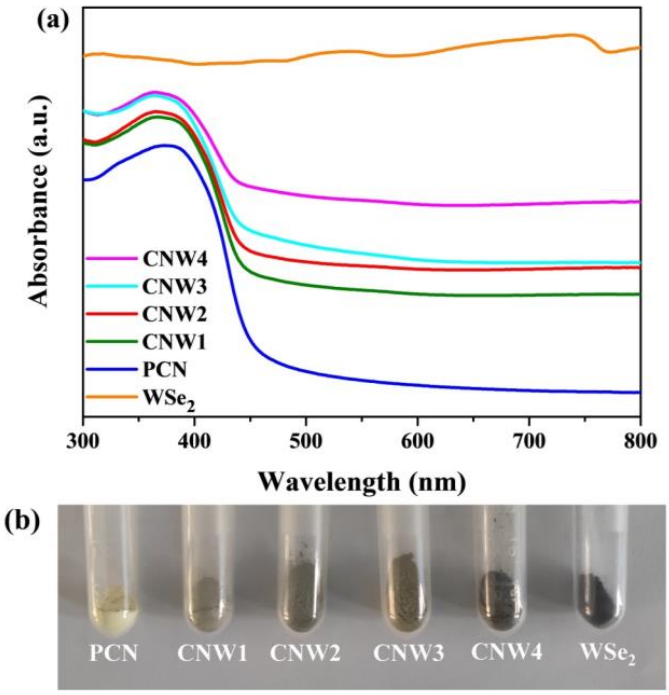

Figure 5. (**a**) UV-vis DRS spectra of PCN, CNW1, CNW2, CNW3, CNW4, and WSe_2; (**b**) color changes of the various samples.

The PL spectra of PCN and CNW2 are shown in Figure 6a. With an excitation wavelength of 369 nm, a strong emission peak appears at around 462 nm of PCN due to rapid recombination of photogenerated electron-hole pairs in PCN. The fluorescence spectrum intensity of the CNW2 composite emission peak becomes significantly lower than that of PCN after WSe_2 loading, indicating that WSe_2 can inhibit the recombination of the electron-hole pairs radiated from PCN. Figure 6b shows the transient photocurrent response curves of the synthesized samples during the typical period of on/off visible light irradiation. The photocurrent is generated immediately after turning on the light, indicating the high photosensitivity and effective space charge separation ability of all samples [54,55]. All of the CNW composites have higher photocurrent response values than PCN, and CNW2 has the highest photocurrent response value with a photocurrent of 0.73 μA cm^{-2}. This means that the appropriate content of WSe_2 can greatly accelerate the separation of charges on the CNW2 sample. The excess black WSe_2 in CNW composites scatters light and produces a shading effect, reducing the utilization of light. In addition, electrochemical impedance spectroscopy was used to examine the conductivity and interface charge transfer behavior of various samples, as shown in Figure 6c. The semicircular diameter of the CNW2 composite material is substantially smaller than that of PCN, indicating that the interface of the CNW2 sample has better conductivity, contributing to the effective separation and transfer of space charge within the CNW2 material during the photocatalytic reaction [56].

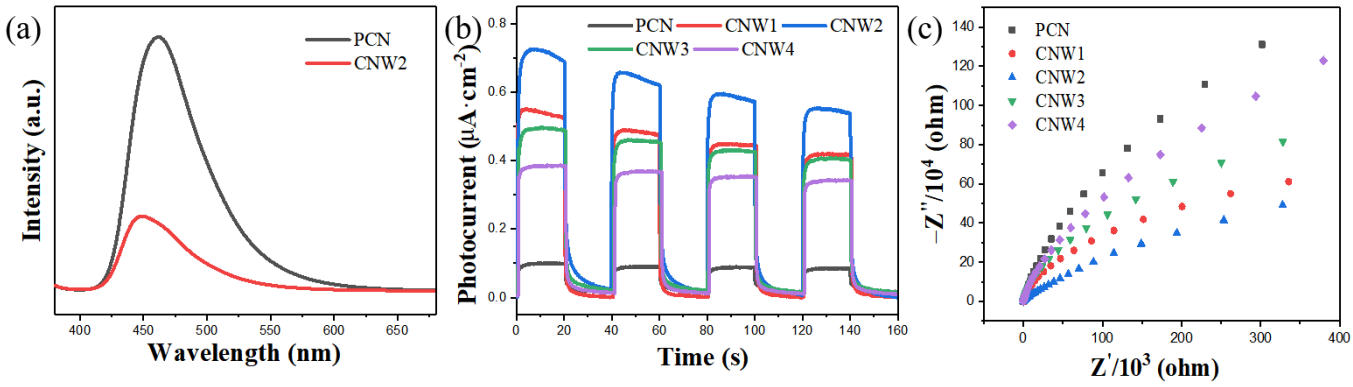

Figure 6. (**a**) PL spectra of PCN and CNW2, (**b**) the transient photocurrent response curves, and (**c**) the electrochemical impedance spectra of PCN, CNW1, CNW2, CNW3, and CNW4.

3.2. Photocatalytic Performances

The photocatalytic performance of the synthesized materials for H_2O_2 production was tested in ultrapure water under visible light. In Figure 7a, the linear coefficient (R^2) of the standard curve is 0.9993, indicating an excellent linear relationship between the concentration of H_2O_2 and its absorbance; as such, use of the absorbance to express the content of hydrogen peroxide is credible. The time course of photocatalytic production of H_2O_2 under visible light irradiation for the synthesized samples is shown in Figure 7b. The rate of H_2O_2 production gradually slows down and finally stabilizes as the reaction progresses, which is caused by the photodecomposition of H_2O_2 [57]. As shown in Figure 7b,c, the H_2O_2 production of pure WSe_2 is 0.97 μmol/L. Under visible light for 2 h, the H_2O_2 production of PCN is about 2.49 μmol/L, suggesting the low H_2O_2 production activity of PCN and the rapid recombination of photogenerated electron-hole pairs [58]. The photocatalytic activity of CNW composite materials is higher than that of PCN and pure WSe_2, indicating that their combination can significantly improve the production of H_2O_2. Among them, CNW2 has the best photocatalytic performance of H_2O_2 generation of 35.04 μmol/L, which is almost 14.1 times higher than that of the original g-C_3N_4 (2.49 μmol/L). Thus, WSe_2 is an effective co-catalyst. However, the production of H_2O_2 gradually decreases as the amount of WSe_2 loading in CNW composites is increased up to 7%. The excessive black WSe_2 in the CNW composite material reduces the utilization of light, thereby reducing the activity of the photocatalytic reaction.

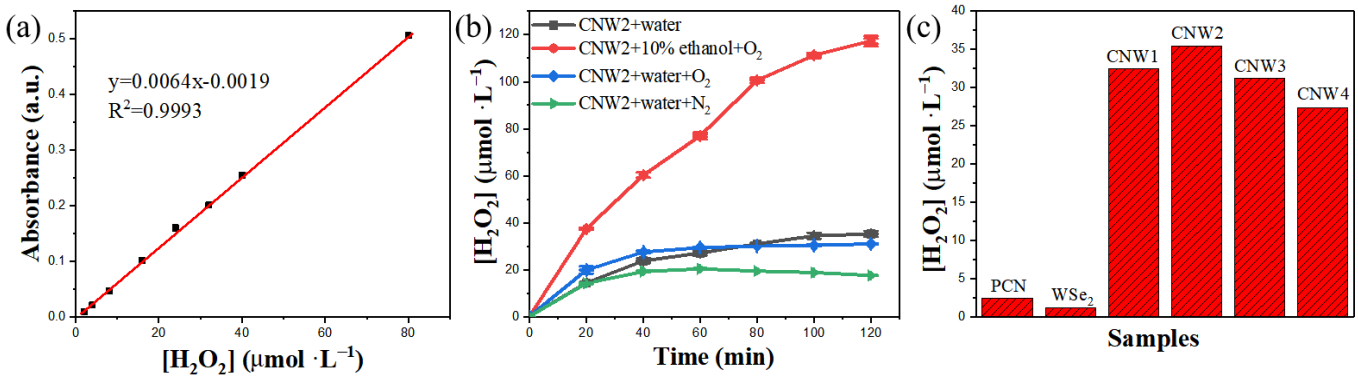

Figure 7. (**a**) Standard curve of the concentration of H_2O_2 and its absorbance, (**b**) photocatalytic H_2O_2 production profiles on various samples under visible light irradiation, and (**c**) maximum yield of H_2O_2 on various samples under visible light irradiation.

The photocatalytic degradation of phenol (10 ppm) by the synthesized samples was performed under visible light. The visible light source in the multi-channel system had a power of 5 W and the reaction lasted 6 h. As shown in Figure 8a, the degradation efficiency of phenol by pure WSe_2 is only about 7%. At the same time, PCN shows poor activity, with phenol degrading at a rate of roughly 25% after 6 h. Under similar conditions, the photocatalytic activity of CNWs is higher than that of PCN. The degradation efficiency rates of the CNW4, CNW3, CNW1, and CNW2 samples are 34%, 52%, 61%, and 67%, respectively. Among them, CNW2 has the best catalytic activity in terms of its behavior in photocatalytic H_2O_2 production. The WSe_2 in CNW2 composites can act as a noble metal-free promoter to increase electron mobility and inhibit the recombination of photo-generated electron-hole pairs, thus increasing the catalytic activity of CNW2.

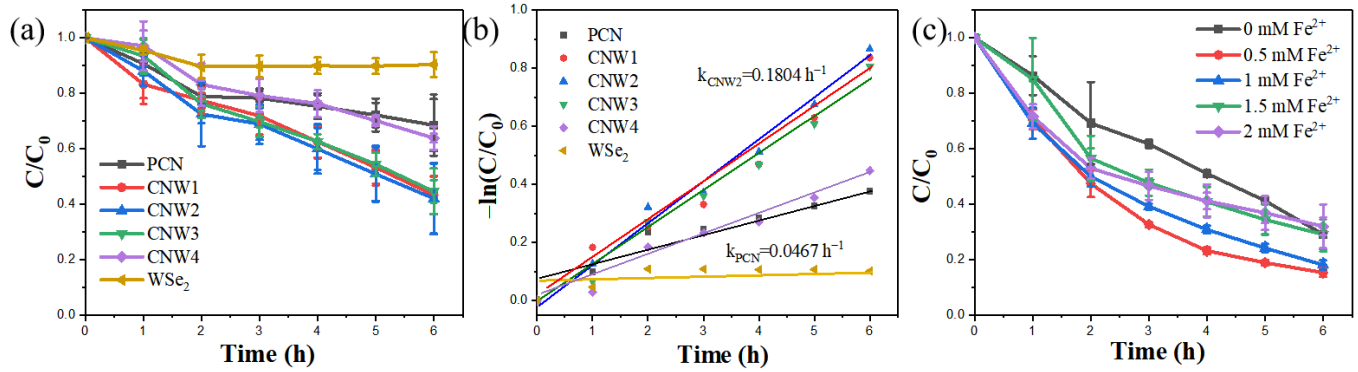

Figure 8. (**a**) Photocatalytic phenol (10 ppm) degradation by the synthesized samples (WSe_2, PCN, CNW1, CNW2, CNW3, and CNW4) under visible light, (**b**) the corresponding kinetic rate constant k (h^{-1}) for photocatalytic degradation of phenol, and (**c**) photocatalytic degradation of phenol (10 ppm) on CNW2 after adding different concentrations of ferrous sulfate heptahydrate under visible light irradiation.

The reaction kinetics of the photocatalytic degradation of phenol were further analyzed using the first order kinetic formula below [59]

$$-\ln\frac{C}{C_0} = k \times t \quad (3)$$

where C, C_0, k, and t, represent the concentration of phenol at time t, the initial concentration of phenol, the reaction rate constant, and the reaction time, respectively.

The kinetic fitting curves of the synthesized samples are shown in Figure 8b, demonstrating that the order of the photocatalytic reaction rate constant (k) of the samples is

WSe_2 < PCN < CNW4 < CNW3 < CNW1 < CNW2. The reaction rate constant of CNW2 increased by about 3.9 times compared to PCN, with respective *k* values of 0.180 h^{-1} and 0.0467 h^{-1}.

The CNW2 composite photocatalyst was chosen for the subsequent in situ photo-Fenton degradation of phenol. The photocatalytic degradation of phenol by CNW2 was investigated at various concentrations of ferrous ions (Fe^{2+}). In the tests, four different concentrations of Fe^{2+} (0.5, 1.0, 1.5, and 2.0 mM) were selected; the results are shown in Figure 8c. The concentration of Fe^{2+} has a significant influence on the photo-Fenton degradation reaction. Adding a proper concentration of Fe^{2+} can increase the degradation of phenol; at an Fe^{2+} concentration of 0.5 mM, phenol degradation is enhanced to 90%. Fe^{2+} activates the H_2O_2 generated by photocatalysis to form an in situ photo-Fenton system by producing more oxidative ·OH and improving photocatalytic degradation efficiency. However, an excessive concentration of Fe^{2+} reduces photocatalytic reaction activity. This may be due to the excessive hydrolysis of Fe^{2+} increasing the acidity of the solution, causing pH to become the dominant factor affecting the photocatalytic reaction. Moreover, compared to the literature (Table S1), the CNW2/Fe^{2+} system has a better phenol degradation rate [60–69].

3.3. Reaction Mechanism

Several control experiments were carried out to clarify the production pathway of H_2O_2 during the photocatalytic reaction shown in Figure 9a. The results show that the production of H_2O_2 can be greatly improved by adding anhydrous ethanol as an electron donor and oxygen gas. When the photocatalytic reaction was carried out in an aqueous ethanol solution with a volume fraction of 10%, the production of H_2O_2 increased from 35.04 μmol L^{-1} (pure water) to 117.32 μmol L^{-1}, nearly 3.35 times higher than that of pure water, within 2 h of light. When oxygen was injected into pure water, the output of H_2O_2 was almost the same as with no gas supplied. At the same time, the production of H_2O_2 was slightly suppressed under the nitrogen atmosphere (simulating an anaerobic environment), which indicates that external oxygen has little influence on the photocatalytic reaction. Generally, oxygen is an essential reactant for the generation of hydrogen peroxide whether through a one-step two-electron direct reduction route or a two-step continuous one-electron indirect reduction route [70]. The valence band of g-C_3N_4 is about 1.4 eV, and its oxidizing property is sufficient to generate oxygen [54]. Therefore, it should be considered that the holes generated in the valence band of g-C_3N_4 in CNW2 can directly oxidize water to generate oxygen. These results indicate that the CNW2 composite material has the potential to generate hydrogen peroxide in an anaerobic environment and can be further used in a variety of other environmental applications, making it a promising photocatalyst.

A coumarin solution was used as a trap to detect the ·OH radicals generated by in situ activation, further confirming the in situ activation of H_2O_2. As shown in Figure 9b,c, after adding Fe^{2+}, the ·OH radical capture product (7-hydroxycoumarin) has a significant peak at about 460 nm and its fluorescence intensity gradually increases with the progress of the reaction. This shows that as the reaction develops the system continuously generates ·OH radicals, accelerating the degradation of phenol. However, in the absence of Fe^{2+}, the characteristic peak of 7-hydroxycoumarin at 460 nm cannot be recognized after 2 h. This indicates that in the absence of Fe^{2+} the amount of ·OH radicals generated by the photocatalytic reaction is almost undetectable. As shown in Figure 9d, the EPR spectra of DMPO spin-trapping adducts for CNW2 dispersion with Fe^{2+} shows stronger signals of ·OH radicals than that without Fe^{2+}, which is consistent with the coumarin capture experiments. Fe^{2+} was able to promote the generation of ·OH radicals. The ·OH radical detection experiment further proved that in combination with Fe^{2+}, the CNW2 photocatalyst could be used to construct an in situ photo-Fenton system for direct phenol degradation without additional H_2O_2.

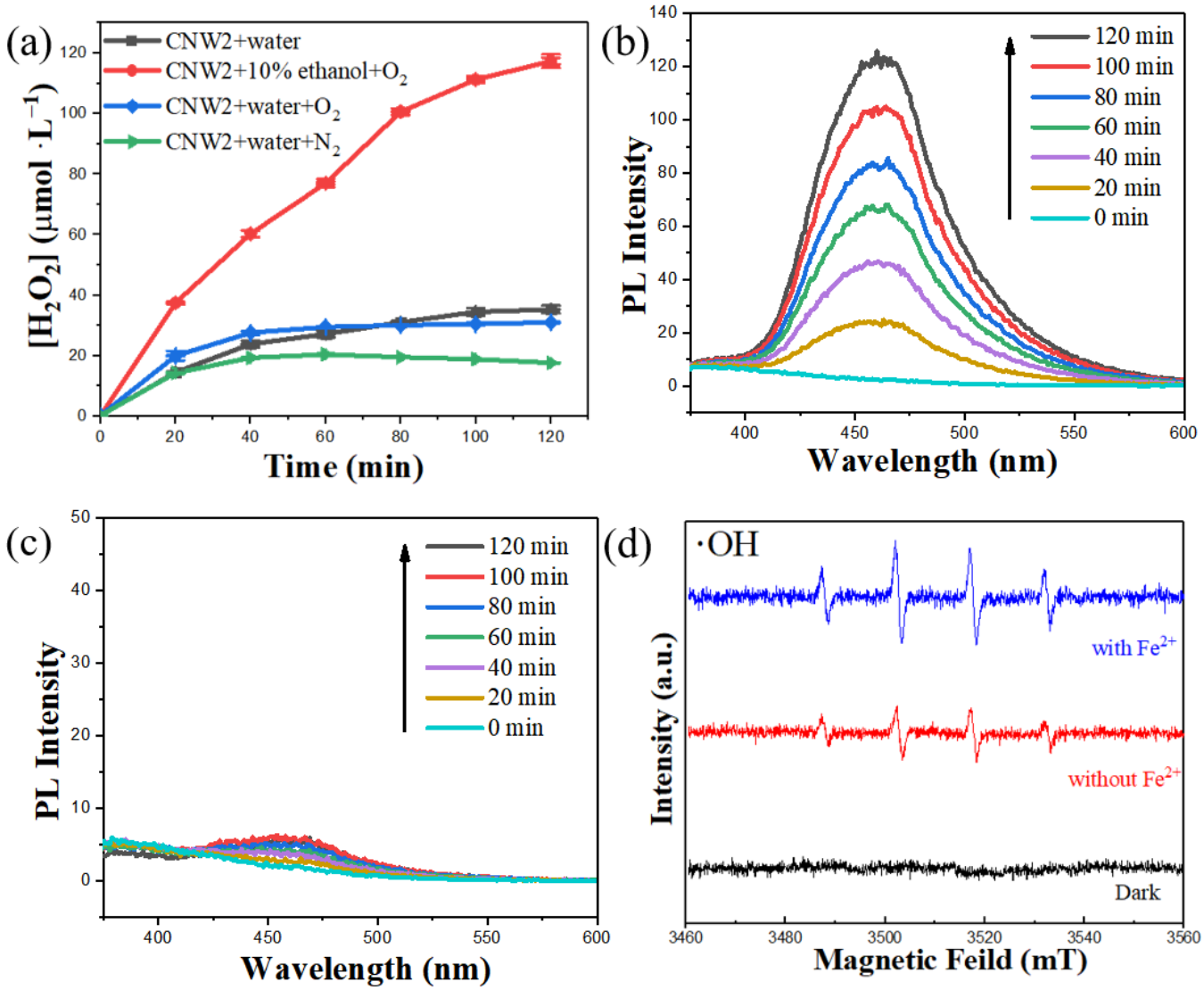

Figure 9. (**a**) Photocatalytic H_2O_2 production under different conditions (including CNW2 + water, CNW2 + 10% ethanol + O_2, and CNW2 + water + O_2, CNW2 + water + N_2) for CNW2, fluorescence spectra of 1 mM coumarin solution (**b**) with Fe^{2+} and (**c**) without Fe^{2+} under visible light irradiation; (**d**) EPR spectra of DMPO spin-trapping adducts for CNW2 dispersion with and without Fe^{2+}.

4. Conclusions

In this work, several WSe_2/g-C_3N_4 photocatalysts with different composite ratios were successfully synthesized by a hydrothermal and calcination method, then characterized by XRD, FTIR, SEM, and TEM. The synthesized samples were applied to photocatalytic H_2O_2 production and photocatalytic degradation of phenol. Among them, CNW2 with 7% loading of WSe_2 displayed the greatest photocatalytic performance with H_2O_2 production of 35.04 μmol/L in two hours, which is about 14.1 times that of PCN. Meanwhile, the phenol degradation efficiency of CNW2 reached 67%, 42% higher than that of PCN. By constructing an in situ photo-Fenton reaction, the addition of 0.5 mM Fe^{2+} was able to further promote the photocatalytic degradation of phenol to 90%. However, there are aspects that can be further studied, such as in the removal of other organic pollutants, the purification of actual polluted water, environmental toxicity, etc. Overall, this work provides new insights for developing new materials for H_2O_2 production in pure water and for in situ photo-Fenton reaction to degrade organic pollutants.

Supplementary Materials: The following supporting information can be downloaded at: https://www.mdpi.com/article/10.3390/nano12183089/s1. Figure S1. TGA plots of PCN, CNW1, CNW2, CNW3 and CNW4. Figure S2. Nitrogen adsorption-desorption isotherm of PCN and CNW2. Figure S3. SEM image and the corresponding EDX elemental mapping images of PCN, CNW3 and CNW4. Figure S4. (a,b) TEM and HRTEM images of PCN, (c,d) TEM and HRTEM images of CNW3, (e,f) TEM and HRTEM images of CNW4. Table S1. Comparison of phenol degradation performance under visible light.

Author Contributions: L.T.: Writing, Methodology, Formal analysis, and Experimental operation, Y.C.: Methodology and Experimental operation, D.L.: Review and Editing, S.W.: Conceptualization, Supervision, Review, Editing and Funding acquisition, Z.A.: Conceptualization, Supervision, Review, Editing and Funding acquisition. All authors have read and agreed to the published version of the manuscript.

Funding: This work was financially supported by the National Natural Science Foundation of China (Grant Nos. 22176041 and 41807191), the Science and Technology Program of Guangdong Province (2017B020216003), and the Innovation Team Project of Guangdong Provincial Department of Education (2017KCXTD012).

Institutional Review Board Statement: Not applicable.

Informed Consent Statement: Not applicable.

Data Availability Statement: Not applicable.

Acknowledgments: Thanks are expressed for the help of the Analysis and Testing Center of Guangdong University of Technology and of Shenzhen Huaxun Testing Technology Co., Ltd., Shenzhen, China.

Conflicts of Interest: The authors declare no conflict of interest.

References

1. Ahn, S.; Song, I.; Choung, Y.; Park, J. Improved phenol degradation in high-phenol-fed MBR by membrane-driven containment of non-settling biodegradation microbes. *Desalination Water Treat.* **2012**, *31*, 320–325. [CrossRef]
2. Emelyanova, E.V.; Solyanikova, I.P. Evaluation of phenol-degradation activity of Rhodococcus opacus 1CP using immobilized and intact cells. *Int. J. Environ. Sci. Technol.* **2020**, *17*, 2279–2294. [CrossRef]
3. Sellaoui, L.; Kehili, M.; Lima, E.C.; Thue, P.S.; Bonilla-Petriciolet, A.; Lamine, A.B.; Dotto, G.L.; Erto, A. Adsorption of phenol on microwave-assisted activated carbons: Modelling and interpretation. *J. Mol. Liq.* **2019**, *274*, 309–314. [CrossRef]
4. Bokare, A.D.; Choi, W. Review of iron-free Fenton-like systems for activating H_2O_2 in advanced oxidation processes. *J. Hazard. Mater.* **2014**, *275*, 121–135. [CrossRef]
5. Clarizia, L.; Russo, D.; Di Somma, I.; Marotta, R.; Andreozzi, R. Homogeneous photo-Fenton processes at near neutral pH: A review. *Appl. Catal. B Environ.* **2017**, *209*, 358–371. [CrossRef]
6. Ayoub, K.; van Hullebusch, E.D.; Cassir, M.; Bermond, A. Application of advanced oxidation processes for TNT removal: A review. *J. Hazard. Mater.* **2010**, *178*, 10–28. [CrossRef]
7. Zepp, R.G.; Faust, B.C.; Hoigne, J. Hydroxyl radical formation in aqueous reactions (pH 3-8) of iron(II) with hydrogen peroxide: The photo-Fenton reaction. *Environ. Sci. Technol.* **1992**, *26*, 313–319. [CrossRef]
8. Li, Y.; Ouyang, S.; Xu, H.; Wang, X.; Bi, Y.; Zhang, Y.; Ye, J. Constructing Solid–Gas-Interfacial Fenton Reaction over Alkalinized-C_3N_4 Photocatalyst to Achieve Apparent Quantum Yield of 49% at 420 nm. *J. Am. Chem. Soc.* **2016**, *138*, 13289–13297. [CrossRef]
9. Zhao, H.; Chen, Y.; Peng, Q.; Wang, Q.; Zhao, G. Catalytic activity of MOF(2Fe/Co)/carbon aerogel for improving H_2O_2 and OH generation in solar photo–electro–Fenton process. *Appl. Catal. B Environ.* **2017**, *203*, 127–137. [CrossRef]
10. Liao, G.; Gong, Y.; Zhang, L.; Gao, H.; Yang, G.-J.; Fang, B. Semiconductor polymeric graphitic carbon nitride photocatalysts: The "holy grail" for the photocatalytic hydrogen evolution reaction under visible light. *Energy Environ. Sci.* **2019**, *12*, 2080–2147. [CrossRef]
11. Huang, D.; Li, Z.; Zeng, G.; Zhou, C.; Xue, W.; Gong, X.; Yan, X.; Chen, S.; Wang, W.; Cheng, M. Megamerger in photocatalytic field: 2D g-C_3N_4 nanosheets serve as support of 0D nanomaterials for improving photocatalytic performance. *Appl. Catal. B Environ.* **2019**, *240*, 153–173. [CrossRef]
12. Tan, L.; Nie, C.; Ao, Z.; Sun, H.; An, T.; Wang, S. Novel two-dimensional crystalline carbon nitrides beyond g-C_3N_4: Structure and applications. *J. Mater. Chem. A* **2021**, *9*, 17–33. [CrossRef]
13. Wang, T.; Nie, C.; Ao, Z.; Wang, S.; An, T. Recent progress in the g-C_3N_4 quantum dots: Synthesis, properties and applications in photocatalytic degradation of organic pollutants. *J. Mater. Chem. A* **2019**, *8*, 485–502. [CrossRef]
14. Shiraishi, Y.; Kanazawa, S.; Sugano, Y.; Tsukamoto, D.; Sakamoto, H.; Ichikawa, S.; Hirai, T. Highly Selective Production of Hydrogen Peroxide on Graphitic Carbon Nitride (g-C_3N_4) Photocatalyst Activated by Visible Light. *ACS Catal.* **2014**, *4*, 774–780. [CrossRef]

15. Cai, J.; Huang, J.; Wang, S.; Iocozzia, J.; Sun, Z.; Sun, J.; Yang, Y.; Lai, Y.; Lin, Z. Crafting Mussel-Inspired Metal Nanoparticle-Decorated Ultrathin Graphitic Carbon Nitride for the Degradation of Chemical Pollutants and Production of Chemical Resources. *Adv. Mater.* **2019**, *31*, 1806314. [CrossRef]
16. Wei, Z.; Liu, M.; Zhang, Z.; Yao, W.; Tan, H.; Zhu, Y. Efficient visible-light-driven selective oxygen reduction to hydrogen peroxide by oxygen-enriched graphitic carbon nitride polymers. *Energy Environ. Sci.* **2018**, *11*, 2581–2589. [CrossRef]
17. Wang, Y.; Jing, B.; Wang, F.; Wang, S.; Liu, X.; Ao, Z.; Li, C. Mechanism Insight into enhanced photodegradation of pharmaceuticals and personal care products in natural water matrix over crystalline graphitic carbon nitrides. *Water Res.* **2020**, *180*, 115925. [CrossRef]
18. Jing, J.; Qi, K.; Dong, G.; Wang, M.; Ho, W. The photocatalytic OH production activity of g-C_3N_4 improved by the introduction of NO. *Chin. Chem. Lett.* **2022**, *33*, 4715–4718. [CrossRef]
19. Wang, W.; Huang, Y.; Wang, Z. Defect Engineering in Two-dimensional Graphitic Carbon Nitride and Application to Photocatalytic Air Purification. *Acta Phys. Chim. Sin.* **2020**, *37*, 2011073. [CrossRef]
20. Li, H.; Li, F.; Yu, J.; Cao, S. 2D/2D FeNi-LDH/g-C3N4 Hybrid Photocatalyst for Enhanced CO_2 Photoreduction. *Acta Phys. Chim. Sin.* **2020**, *37*, 2010073. [CrossRef]
21. Bertolazzi, S.; Gobbi, M.; Zhao, Y.; Backes, C.; Samorì, P. Molecular chemistry approaches for tuning the properties of two-dimensional transition metal dichalcogenides. *Chem. Soc. Rev.* **2018**, *47*, 6845–6888. [CrossRef] [PubMed]
22. Yu, M.; Liang, H.; Zhan, R.; Xu, L.; Niu, J. Sm-doped g-C_3N_4/Ti_3C_2 MXene heterojunction for visible-light photocatalytic degradation of ciprofloxacin. *Chin. Chem. Lett.* **2021**, *32*, 2155–2158. [CrossRef]
23. Ye, L.; Wang, P.; Luo, W.; Gong, F.; Liao, L.; Liu, T.; Tong, L.; Zang, J.; Xu, J.; Hu, W. Highly polarization sensitive infrared photodetector based on black phosphorus-on-WSe_2 photogate vertical heterostructure. *Nano Energy* **2017**, *37*, 53–60. [CrossRef]
24. Liu, B.; Ma, Y.; Zhang, A.; Chen, L.; Abbas, A.N.; Liu, Y.; Shen, C.; Wan, H.; Zhou, C. High-Performance WSe_2 Field-Effect Transistors via Controlled Formation of In-Plane Heterojunctions. *ACS Nano* **2016**, *10*, 5153–5160. [CrossRef]
25. Xu, J.; Shim, J.; Park, J.-H.; Lee, S. MXene Electrode for the Integration of WSe_2 and MoS_2 Field Effect Transistors. *Adv. Funct. Mater.* **2016**, *26*, 5328–5334. [CrossRef]
26. Biswas, M.R.U.D.; Ali, A.; Cho, K.Y.; Oh, W.-C. Novel synthesis of WSe_2-Graphene-TiO_2 ternary nanocomposite via ultrasonic technics for high photocatalytic reduction of CO_2 into CH_3OH. *Ultrason. Sonochem.* **2018**, *42*, 738–746. [CrossRef]
27. Zhu, L.; Nguyen, D.C.T.; Woo, J.-H.; Zhang, Q.; Cho, K.Y.; Oh, W.-C. An eco-friendly synthesized mesoporous-silica particle combined with WSe_2-graphene-TiO_2 by self-assembled method for photocatalytic dye decomposition and hydrogen production. *Sci. Rep.* **2018**, *8*, 12759. [CrossRef]
28. Guo, X.; Guo, P.; Wang, C.; Chen, Y.; Guo, L. Few-layer WSe_2 nanosheets as an efficient cocatalyst for improved photocatalytic hydrogen evolution over Zn0.1Cd0.9S nanorods. *Chem. Eng. J.* **2020**, *383*, 123183. [CrossRef]
29. Lin, Z.; Li, J.; Zheng, Z.; Li, L.; Yu, L.; Wang, C.; Yang, G. A Floating Sheet for Efficient Photocatalytic Water Splitting. *Adv. Energy Mater.* **2016**, *6*, 1600510. [CrossRef]
30. Wang, W.; Gu, W.; Li, G.; Xie, H.; Wong, P.K.; An, T. Few-layered tungsten selenide as a co-catalyst for visible-light-driven photocatalytic production of hydrogen peroxide for bacterial inactivation. *Environ. Sci. Nano* **2020**, *7*, 3877–3887. [CrossRef]
31. Zhang, Y.; Pan, Q.; Chai, G.; Liang, M.; Dong, G.; Zhang, Q.; Qiu, J. Synthesis and luminescence mechanism of multicolor-emitting g-C_3N_4 nanopowders by low temperature thermal condensation of melamine. *Sci. Rep.* **2013**, *3*, 1943. [CrossRef] [PubMed]
32. Chen, Y.; Gu, W.; Tan, L.; Ao, Z.; An, T.; Wang, S. Photocatalytic H_2O_2 production using Ti_3C_2 MXene as a non-noble metal cocatalyst. *Appl. Catal. A Gen.* **2021**, *618*, 118127. [CrossRef]
33. Liu, W.; Nie, C.; Li, W.; Ao, Z.; Wang, S.; An, T. Oily sludge derived carbons as peroxymonosulfate activators for removing aqueous organic pollutants: Performances and the key role of carbonyl groups in electron-transfer mechanism. *J. Hazard. Mater.* **2021**, *414*, 125552. [CrossRef] [PubMed]
34. Wang, W.; Wang, H.; Li, G.; An, T.; Zhao, H.; Wong, P.K. Catalyst-free activation of persulfate by visible light for water disinfection: Efficiency and mechanisms. *Water Res.* **2019**, *157*, 106–118. [CrossRef]
35. Muska, M.; Yang, J.; Sun, Y.; Wang, J.; Wang, Y.; Yang, Q. $CoSe_2$ Nanoparticles Dispersed in WSe2 Nanosheets for Efficient Electrocatalysis and Supercapacitance Applications. *ACS Appl. Nano Mater.* **2021**, *4*, 5796–5807. [CrossRef]
36. Zhou, C.; Lai, C.; Huang, D.; Zeng, G.; Zhang, C.; Cheng, M.; Hu, L.; Wan, J.; Xiong, W.; Wen, M.; et al. Highly porous carbon nitride by supramolecular preassembly of monomers for photocatalytic removal of sulfamethazine under visible light driven. *Appl. Catal. B Environ.* **2018**, *220*, 202–210. [CrossRef]
37. Wang, W.; Zeng, Z.; Zeng, G.; Zhang, C.; Xiao, R.; Zhou, C.; Xiong, W.; Yang, Y.; Lei, L.; Liu, Y.; et al. Sulfur doped carbon quantum dots loaded hollow tubular g-C_3N_4 as novel photocatalyst for destruction of Escherichia coli and tetracycline degradation under visible light. *Chem. Eng. J.* **2019**, *378*, 122132. [CrossRef]
38. Yang, Y.; Zhang, C.; Huang, D.; Zeng, G.; Huang, J.; Lai, C.; Zhou, C.; Wang, W.; Guo, H.; Xue, W.; et al. Boron nitride quantum dots decorated ultrathin porous g-C_3N_4: Intensified exciton dissociation and charge transfer for promoting visible-light-driven molecular oxygen activation. *Appl. Catal. B Environ.* **2019**, *245*, 87–99. [CrossRef]
39. Zhou, C.; Xu, P.; Lai, C.; Zhang, C.; Zeng, G.; Huang, D.; Cheng, M.; Hu, L.; Xiong, W.; Wen, X.; et al. Rational design of graphic carbon nitride copolymers by molecular doping for visible-light-driven degradation of aqueous sulfamethazine and hydrogen evolution. *Chem. Eng. J.* **2019**, *359*, 186–196. [CrossRef]

40. Yu, B.; Zheng, B.; Wang, X.; Qi, F.; He, J.; Zhang, W.; Chen, Y. Enhanced photocatalytic properties of graphene modified few-layered WSe_2 nanosheets. *Appl. Surf. Sci.* **2017**, *400*, 420–425. [CrossRef]
41. Wang, X.; Chen, Y.; Zheng, B.; Qi, F.; He, J.; Li, Q.; Li, P.; Zhang, W. Graphene-like WSe_2 nanosheets for efficient and stable hydrogen evolution. *J. Alloys Compd.* **2017**, *691*, 698–704. [CrossRef]
42. Li, J.; Shen, B.; Hong, Z.; Lin, B.; Gao, B.; Chen, Y. A facile approach to synthesize novel oxygen-doped g-C_3N_4 with superior visible-light photoreactivity. *Chem. Commun.* **2012**, *48*, 12017. [CrossRef] [PubMed]
43. Lin, Z.; Wang, X. Nanostructure Engineering and Doping of Conjugated Carbon Nitride Semiconductors for Hydrogen Photosynthesis. *Angew. Chem. Int. Ed.* **2013**, *52*, 1735–1738. [CrossRef] [PubMed]
44. Wu, Y.; Wang, H.; Tu, W.; Wu, S.; Liu, Y.; Tan, Y.Z.; Luo, H.; Yuan, X.; Chew, J.W. Petal-like CdS nanostructures coated with exfoliated sulfur-doped carbon nitride via chemically activated chain termination for enhanced visible-light–driven photocatalytic water purification and H_2 generation. *Appl. Catal. B Environ.* **2018**, *229*, 181–191. [CrossRef]
45. Dong, G.; Zhao, K.; Zhang, L. Carbon self-doping induced high electronic conductivity and photoreactivity of g-C_3N_4. *Chem. Commun.* **2012**, *48*, 6178. [CrossRef]
46. Zhou, C.; Huang, D.; Xu, P.; Zeng, G.; Huang, J.; Shi, T.; Lai, C.; Zhang, C.; Cheng, M.; Lu, Y.; et al. Efficient visible light driven degradation of sulfamethazine and tetracycline by salicylic acid modified polymeric carbon nitride via charge transfer. *Chem. Eng. J.* **2019**, *370*, 1077–1086. [CrossRef]
47. Huang, D.; Sun, X.; Liu, Y.; Ji, H.; Liu, W.; Wang, C.-C.; Ma, W.; Cai, Z. A carbon-rich g-C_3N_4 with promoted charge separation for highly efficient photocatalytic degradation of amoxicillin. *Chin. Chem. Lett.* **2021**, *32*, 2787–2791. [CrossRef]
48. Zhang, N.; Li, X.; Liu, Y.; Long, R.; Li, M.; Chen, S.; Qi, Z.; Wang, C.; Song, L.; Jiang, J.; et al. Defective Tungsten Oxide Hydrate Nanosheets for Boosting Aerobic Coupling of Amines: Synergistic Catalysis by Oxygen Vacancies and Brønsted Acid Sites. *Small* **2017**, *13*, 1701354. [CrossRef]
49. Guo, J.; Shi, Y.; Bai, X.; Wang, X.; Ma, T. Atomically thin $MoSe_2$/graphene and WSe_2/graphene nanosheets for the highly efficient oxygen reduction reaction. *J. Mater. Chem. A* **2015**, *3*, 24397–24404. [CrossRef]
50. Zhang, S.; Wang, C.-G.; Li, M.-Y.; Huang, D.; Li, L.-J.; Ji, W.; Wu, S. Defect Structure of Localized Excitons in a WSe_2 Monolayer. *Phys. Rev. Lett.* **2017**, *119*, 046101. [CrossRef]
51. Zhang, T.; Su, J.; Guo, L. Morphology engineering of WO_3/$BiVO_4$ heterojunctions for efficient photocatalytic water oxidation. *CrystEngComm* **2016**, *18*, 8961–8970. [CrossRef]
52. Liu, Z.; Zhao, H.; Li, N.; Zhang, Y.; Zhang, X.; Du, Y. Assembled 3D electrocatalysts for efficient hydrogen evolution: WSe_2 layers anchored on graphene sheets. *Inorg. Chem. Front.* **2016**, *3*, 313–319. [CrossRef]
53. Zou, M.; Zhang, J.; Zhu, H.; Du, M.; Wang, Q.; Zhang, M.; Zhang, X. A 3D dendritic WSe_2 catalyst grown on carbon nanofiber mats for efficient hydrogen evolution. *J. Mater. Chem. A* **2015**, *3*, 12149–12153. [CrossRef]
54. Lin, Y.; Wu, S.; Yang, C.; Chen, M.; Li, X. Preparation of size-controlled silver phosphate catalysts and their enhanced photocatalysis performance via synergetic effect with MWCNTs and PANI. *Appl. Catal. B Environ.* **2019**, *245*, 71–86. [CrossRef]
55. Xue, W.; Peng, Z.; Huang, D.; Zeng, G.; Wen, X.; Deng, R.; Yang, Y.; Yan, X. In situ synthesis of visible-light-driven Z-scheme AgI/Bi_2WO_6 heterojunction photocatalysts with enhanced photocatalytic activity. *Ceram. Int.* **2019**, *45*, 6340–6349. [CrossRef]
56. Wen, R.; Yang, L.; Wu, S.; Zhou, D.; Jiang, B. Tuning surface sites to boost photocatalytic degradation of phenol and ciprofloxacin. *Chin. Chem. Lett.* 2022; *in press*. [CrossRef]
57. Haider, Z.; Cho, H.-I.; Moon, G.-H.; Kim, H.-I. Minireview: Selective production of hydrogen peroxide as a clean oxidant over structurally tailored carbon nitride photocatalysts. *Catal. Today* **2019**, *335*, 55–64. [CrossRef]
58. Chu, S.; Wang, Y.; Guo, Y.; Feng, J.; Wang, C.; Luo, W.; Fan, X.; Zou, Z. Band Structure Engineering of Carbon Nitride: In Search of a Polymer Photocatalyst with High Photooxidation Property. *ACS Catal.* **2013**, *3*, 912–919. [CrossRef]
59. Wang, W.; Li, X.; Deng, F.; Liu, J.; Gao, X.; Huang, J.; Xu, J.; Feng, Z.; Chen, Z.; Han, L. Novel organic/inorganic PDI-Urea/BiOBr S-scheme heterojunction for improved photocatalytic antibiotic degradation and H_2O_2 production. *Chin. Chem. Lett.* **2022**, *33*, 5200–5207. [CrossRef]
60. Zhang, J.; Zheng, Y.; Ma, M.; Li, H. Structural Characterization and Photocatalytic Activity of Synthesized Carbon Modified TiO_2 for Phenol Degradation. *J. Wuhan Univ. Technol.-Mat. Sci. Edit.* **2020**, *35*, 535–540. [CrossRef]
61. Vasallo-Antonio, R.; Peña-Bahamonde, J.; Susman, M.D.; Ballesteros, F.C.; Rodrigues, D.F. Design and performance of Fe_3O_4@SiO_2/MoO_3/polydopamine-graphene oxide composites for visible light photocatalysis. *Emergent Mater.* **2021**, *4*, 1425–1439. [CrossRef]
62. Firdharini, C.; Setyaningtyas, T.; Riyani, K. Comparative study of Fe^{2+}/H_2O_2/CuO/Vis and Fe^{2+}/H_2O_2/CuO for phenol removal in batik wastewater under visible light irradiation. *J. Phys. Conf. Ser.* **2021**, *1918*, 032004. [CrossRef]
63. Lee, S.C.; Lintang, H.O.; Endud, S.; Yuliati, L. Highly Active Mesoporous Carbon Nitride for Removal of Aromatic Organic Pollutants under Visible Light Irradiation. *Adv. Mater. Res.* **2014**, *925*, 130–134. [CrossRef]
64. Trinh, D.T.T.; Channei, D.; Nakaruk, A.; Khanitchaidecha, W. New insight into the photocatalytic degradation of organic pollutant over $BiVO_4$/SiO_2/GO nanocomposite. *Sci. Rep.* **2021**, *11*, 4620. [CrossRef]
65. Asencios, Y.J.O.; Lourenço, V.S.; Carvalho, W.A. Removal of phenol in seawater by heterogeneous photocatalysis using activated carbon materials modified with TiO_2. *Catal. Today* **2022**, *388–389*, 247–258. [CrossRef]

66. Nawaz, R.; Haider, S.; Ullah, H.; Akhtar, M.S.; Khan, S.; Junaid, M.; Khan, N. Optimized remediation of treated agro-industrial effluent using visible light-responsive core-shell structured black TiO_2 photocatalyst. *J. Environ. Chem. Eng.* **2022**, *10*, 106968. [CrossRef]
67. Wu, G.; Xing, W. Facile Preparation of Semiconductor Silver Phosphate Loaded on Multi-walled Carbon Nanotube Surface and Its Enhanced Catalytic Performance. *J. Inorg. Organomet. Polym.* **2018**, *29*, 617–627. [CrossRef]
68. Lee, S.C.; Lintang, H.O.; Yuliati, L. A urea precursor to synthesize carbon nitride with mesoporosity for enhanced activity in the photocatalytic removal of phenol. *Chem. Asian J.* **2012**, *7*, 2139–2144. [CrossRef]
69. Hu, J.Y.; Tian, K.; Jiang, H. Improvement of phenol photodegradation efficiency by a combined g-C_3N_4/Fe(III)/persulfate system. *Chemosphere* **2016**, *148*, 34–40. [CrossRef]
70. Moon, G.-H.; Kim, W.; Bokare, A.D.; Sung, N.-E.; Choi, W. Solar production of H_2O_2 on reduced graphene oxide–TiO_2 hybrid photocatalysts consisting of earth-abundant elements only. *Energy Environ. Sci.* **2014**, *7*, 4023–4028. [CrossRef]